

Advanced 3D Monte Carlo algorithms for bio-photonic and medical applications

Lewis McMillan



University of
St Andrews

This thesis is submitted in partial fulfilment for the degree of
PhD
at the
University of St Andrews

March 2019

Declaration

I, Lewis McMillan, hereby certify that this thesis, which is approximately ***** words in length, has been written by me, that it is the record of work carried out by me, or principally by myself in collaboration with others as acknowledged, and that it has not been submitted in any previous application for a higher degree.

I was admitted as a research student in September 2015 and as a candidate for the degree of PhD in September 2015; the higher study for which this is a record was carried out in the University of St Andrews between 2015 and 2019.

Date Signature of candidate

I hereby certify that the candidate has fulfilled the conditions of the Resolution and Regulations appropriate for the degree of PhD in the University of St Andrews and that the candidate is qualified to submit this thesis in application for that degree.

Date Signature of supervisor

Date Signature of supervisor

Abstract

Lorem ipsum dolor sit amet, consectetur adipiscing elit. Ut purus elit, vestibulum ut, placerat ac, adipiscing vitae, felis. Curabitur dictum gravida mauris. Nam arcu libero, nonummy eget, consectetur id, vulputate a, magna. Donec vehicula augue eu neque. Pellentesque habitant morbi tristique senectus et netus et malesuada fames ac turpis egestas. Mauris ut leo. Cras viverra metus rhoncus sem. Nulla et lectus vestibulum urna fringilla ultrices. Phasellus eu tellus sit amet tortor gravida placerat. Integer sapien est, iaculis in, pretium quis, viverra ac, nunc. Praesent eget sem vel leo ultrices bibendum. Aenean faucibus. Morbi dolor nulla, malesuada eu, pulvinar at, mollis ac, nulla. Curabitur auctor semper nulla. Donec varius orci eget risus. Duis nibh mi, congue eu, accumsan eleifend, sagittis quis, diam. Duis eget orci sit amet orci dignissim rutrum.

Nam dui ligula, fringilla a, euismod sodales, sollicitudin vel, wisi. Morbi auctor lorem non justo. Nam lacus libero, pretium at, lobortis vitae, ultricies et, tellus. Donec aliquet, tortor sed accumsan bibendum, erat ligula aliquet magna, vitae ornare odio metus a mi. Morbi ac orci et nisl hendrerit mollis. Suspendisse ut massa. Cras nec ante. Pellentesque a nulla. Cum sociis natoque penatibus et magnis dis parturient montes, nascetur ridiculus mus. Aliquam tincidunt urna. Nulla ullamcorper vestibulum turpis. Pellentesque cursus luctus mauris.

Acknowledgements

Lorem ipsum dolor sit amet, consectetur adipiscing elit. Ut purus elit, vestibulum ut, placerat ac, adipiscing vitae, felis. Curabitur dictum gravida mauris. Nam arcu libero, nonummy eget, consectetur id, vulputate a, magna. Donec vehicula augue eu neque. Pellentesque habitant morbi tristique senectus et netus et malesuada fames ac turpis egestas. Mauris ut leo. Cras viverra metus rhoncus sem. Nulla et lectus vestibulum urna fringilla ultrices. Phasellus eu tellus sit amet tortor gravida placerat. Integer sapien est, iaculis in, pretium quis, viverra ac, nunc. Praesent eget sem vel leo ultrices bibendum. Aenean faucibus. Morbi dolor nulla, malesuada eu, pulvinar at, mollis ac, nulla. Curabitur auctor semper nulla. Donec varius orci eget risus. Duis nibh mi, congue eu, accumsan eleifend, sagittis quis, diam. Duis eget orci sit amet orci dignissim rutrum.

Nam dui ligula, fringilla a, euismod sodales, sollicitudin vel, wisi. Morbi auctor lorem non justo. Nam lacus libero, pretium at, lobortis vitae, ultricies et, tellus. Donec aliquet, tortor sed accumsan bibendum, erat ligula aliquet magna, vitae ornare odio metus a mi. Morbi ac orci et nisl hendrerit mollis. Suspendisse ut massa. Cras nec ante. Pellentesque a nulla. Cum sociis natoque penatibus et magnis dis parturient montes, nascetur ridiculus mus. Aliquam tincidunt urna. Nulla ullamcorper vestibulum turpis. Pellentesque cursus luctus mauris.

Contents

Declaration	iii
Abstract	v
Acknowledgements	vii
List of Figures	xii
1 Monte Carlo radiation transport technique	1
1.1 Introduction and Background	1
1.1.1 Monte Carlo method	1
1.2 Monte Carlo radiation transport algorithm	2
1.2.1 Introduction & background	2
1.2.2 MCRT algorithm	2
1.2.2.1 Grid set-up	3
1.2.2.2 Photon launch	3
1.2.2.3 Photon move	4
1.2.2.4 Photon scatter and absorbing	5
1.2.2.5 Termination	5
1.2.3 Code details	5
1.3 Validation of MCRT code	5
1.4 Optical properties	5
1.5 Further extensions to the code	5
2 Computational modelling of tissue ablation	7
2.1 Introduction and background	7
2.2 Methods	7
2.2.1 Monte Carlo radiation transport (MCRT)	8
2.2.2 Heat transport	11
2.2.3 Tissue Damage	16
2.2.3.1 Introduction	16
2.2.3.2 Modelling coagulation damage	18
2.2.3.3 Modelling physical tissue damage	18
2.2.4 Validation	19
2.2.4.1 Heat transport validation	19
2.2.4.2 MCRT & heat transport validation	21
2.3 <i>In silico</i> results	21
2.3.1 Introduction	21

2.3.1.1	Optical & thermal properties	21
2.3.1.2	Computational speed up:	23
2.3.2	Results	24
2.3.2.1	Investigating ablation temperature, T_a	24
2.3.2.2	Investigating Thermal damage	25
2.3.2.3	Comparison to experimental work	25
2.3.2.4	Effect of beam shape	26
2.3.2.5	Effect of thermal and optical properties on crater depth	26
2.3.2.6	Investigating water content	27
2.3.2.7	Investigating temperature of air after ablation	27
2.4	Conclusion	27

List of Figures

1.1	Sample buffon needle experiment. 100 needles are dropped on a 10 by 10 cm area with lines spaced 1.5cm apart. If a needle lands on a line it is recorded and colored blue, else it is yellow. This simulation gave a value of pi as 3.17.	2
1.2	Computer generated imagery using ray-tracing. Code usd to create image available at: https://github.com/lewisfish/RayTran	3
2.1	Example of a possible voxel model, with three different layers, various holes due to ablative pixel beam lasers. Each voxel can represent a different optical/thermal property of the tissue medium.	8
2.2	Flowchart of the tissue ablation algorithm.	10
2.3	Red lines are photon paths within a voxel. Black lines photon paths outwith the voxel. Red photon paths are summed up in order to calculate the absorbed energy within each voxel.	10
2.4	Discretisation of $f(x)$.	12
2.5	Finite difference method stencil for simple explicit scheme	13
2.6	Computational domain decomposition. Total computational domain (red outline) is evenly divided between cores in the CPU. This is done via layers of the domain in the z direction. Information is passed to/from cores via the ‘halo swap’ process (see Fig. 2.7).	15
2.7	Halo swapping. Process A updates the area in red and blue on the left. It updates the blue area which is sent to process B as B’s ‘halo’. Process B cannot update its own halo, but rather updates the halo for process A.	16
2.8	Tissue ablations, as viewed under a microscope. Steam vacuoles are clearly visible either side of the ablation area. Carbonisation is also evident at the edges of the ablation fronts. Adapted from [1].	17
2.9	Comparison between analytical solution and numerical method.	20
2.10	Water absorption coefficient for wavelengths 0-12000nm [2]. Data shows that water is highly absorbing in the infra-red portion of the spectrum compared to the visible portion.	22
2.11	Simulation of 81 pixel beams. Figure is a slice through the optical properties at the end of the simulation. Yellow is unchanged tissue, and purple is completely ablated tissue. Figure shows that the ablation craters do not overlap one another.	23
2.12	Simulations of 30 W and 70 W CO ₂ ablative laser. Crater depths as a function of pixel beam energy for various ablation temperature (T_a)’s. *placeholder until I get 70W dundee data. need to rerun the upper 177 points on larger z depth as it crashes currently due to known error*	24

2.13	Tissue thermal damage around the ablation crater (white). Thermal tissue damage values of 3 refer to 3 rd degree burns, 2 to 2 nd , and 1 to 1 st degree burns respectively. P is the power in Watts, T_a is the ablation temperature in Kelvin, and E_p is the energy per pixel beam in mJ *need to do this with more voxels*.	26
2.14	Figure shows the maximum horizontal extent of thermal damage as a function of energy per pixel beam for laser of power 30 W. Cut-off in thermal damage appears to set in around 250 mJ .	27
2.15	Figure shows the maximum horizontal extent of thermal damage as a function of energy per pixel beam for laser of power 70 W. There appears to be not cut-off in the horizontal extent of the thermal damage. *need to do this with more voxels*	28
2.16	Figure shows the extent of burns inflicted by the laser as a function of depth. Lines are taken from the central point of the laser beam through the tissue. Coloured dashed lines are 30W laser and solid coloured lines are 70W laser.	29

Chapter 1

Monte Carlo radiation transport technique

1.1 Introduction and Background

This chapter will provide an overview of the Monte Carlo method and how it is used within the context of [Monte Carlo radiation Transfer \(MCRT\)](#). The chapter will then present the details of the MCRT code used as the basis of the subsequent chapters. Validation of this code and details of computational speed up are also presented. Subsequent chapters will expand upon the code for each individual projects needs.

1.1.1 Monte Carlo method

The Monte Carlo method is a numerical analysis technique based upon random numbers, which are used to calculate unknown variables in problems.

The earliest use of the method is in Buffon's needle experiment of the 18th century [3–5]. Buffon asked the question;

“Suppose we have a floor made of parallel strips of wood, each the same width, and we drop a needle onto the floor. What is the probability that the needle will lie across a line between two strips?”

The solution to this question is as: for a needle length l , strip separation s , and where x is the distance from the needle to the closest line. Then using a simple geometrical argument, a needle crosses a strip if $x \leq \frac{l}{2} \sin\theta$.

x is distributed uniformly in $[0, \frac{s}{2}]$, and θ in $[0, \frac{\pi}{2}]$. Therefore the probability density function for x is $p(x) = \frac{2}{s}$, and θ is $p(\theta) = \frac{2}{\pi}$. The [probability density function \(PDF\)](#), is a function of a variable that gives probability for a variable to take a given value. The [PDF](#) is normalised over the whole range of the variable, in this case x , and θ . Thus, as x and θ are independent variables, giving a joint probability of $p(x, \theta) = \frac{4}{s\pi}$. So the probability of a needle of length l ($l < s$) is:

$$P = \int_0^{\frac{\pi}{2}} \int_0^{\frac{l}{2} \sin\theta} \frac{4}{s\pi} dx d\theta = \frac{2l}{s\pi} \quad (1.1)$$

Equation (1.1) can be used to carry out a Monte Carlo estimation of pi. A simple rearrangement yields: $\pi = \frac{2l}{sP}$ where P is the ratio of needles crossing the line over total number dropped.

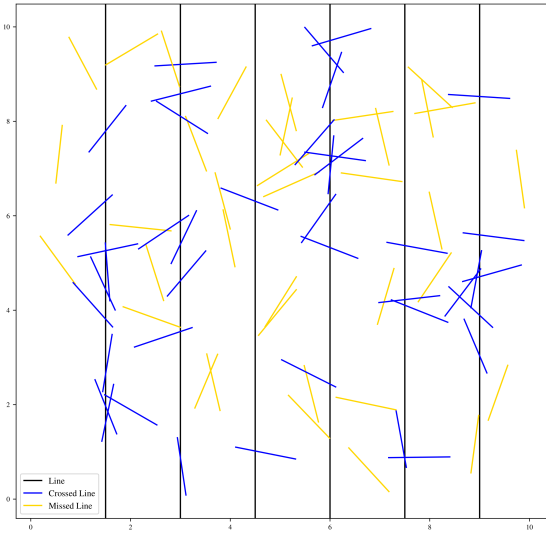


Figure 1.1: Sample buffon needle experiment. 100 needles are dropped on a 10 by 10 cm area with lines spaced 1.5cm apart. If a needle lands on a line it is recorded and colored blue, else it is yellow. This simulation gave a value of π as 3.17.

Laplace was the first to suggest that Buffon's needle experiment could be used to estimate π [4]. Figure 1.1 shows an example of simulation of Buffon's needle experiment.

The Monte Carlo method is used in various different disciplines. Ranging from use in the financial sector to analyse investments and stocks by simulating the sources of uncertainty which affect their values [6, 7], use in statistical analysis [8], and in modern computer generated images (see Fig. 1.2) [9, 10].

1.2 Monte Carlo radiation transport algorithm

1.2.1 Introduction & background

The technique that makes up the bulk of this thesis, is the MCRT technique. This method was developed at the tail end of World War two at the Los Alamos National Laboratory, for the purpose of calculating neutron diffusion through shielding material [11–14]. It has since found a myriad of applications from light transport through dusty clouds [15], calculating doses for radiotherapy [16] to light transport through tissue [17].

1.2.2 MCRT algorithm

The MCRT algorithm can be as simple as a ~ 20 line program to as complex as needed for the problem at hand. This section will provide a detailed description a simple MCRT algorithm for a 3D voxel based grid.

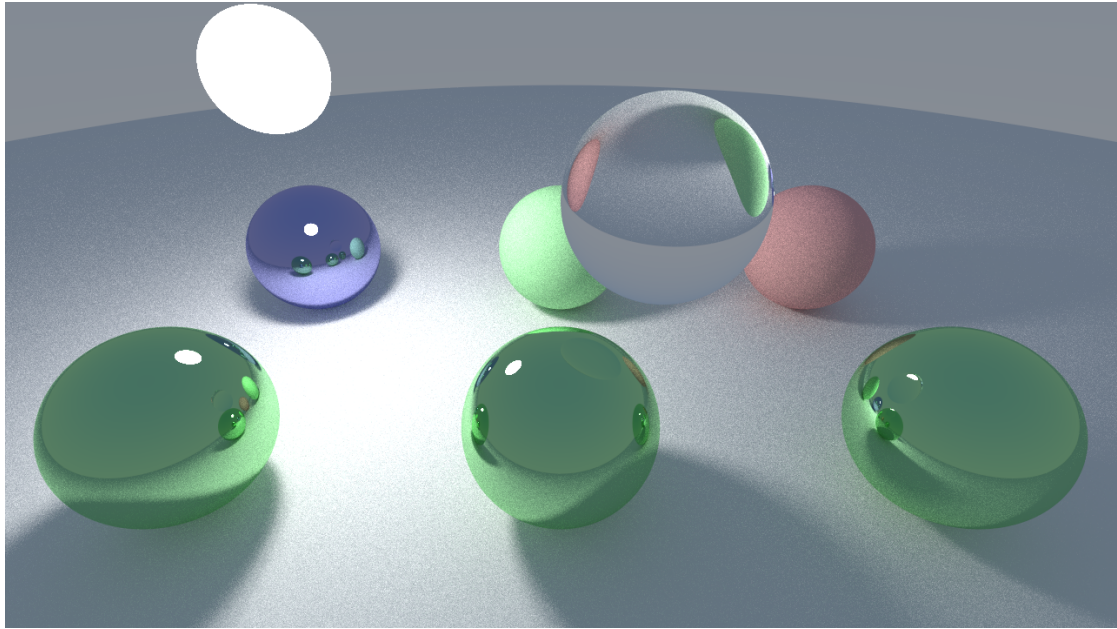


Figure 1.2: Computer generated imagery using ray-tracing. Code used to create image available at: <https://github.com/lewisfish/RayTran>

1.2.2.1 Grid set-up

The first step of the MCRT algorithm is to set-up the grid which acts as the simulated medium. This grid consists of $n \times n \times n$ voxels¹ of which each voxel has its own optical properties. This allows the medium of interest to be discretised onto a grid, which gives a good approximation of the real-life medium (see Section 1.5 for discussion on this). Once the medium has been set-up photon packets are launched and propagated through the voxel structure.

1.2.2.2 Photon launch

The initial step of any MCRT algorithm is to launch a photon packet. Depending on the source of photon packets for a given simulation, this step varies from simulation to simulation. The general idea of launching a photon packet is that the packet is given an initial direction vector and position (which consists of a physical position and a voxel position)²:

$$direction = \begin{bmatrix} n_{xp} \\ n_{yp} \\ n_{zp} \end{bmatrix} \quad (1.2)$$

$$position = [x_p, y_p, z_p] \quad (1.3)$$

$$voxel = [x_{cell}, y_{cell}, z_{cell}] \quad (1.4)$$

In order to set the direction vectors, the components of the direction vectors must be first set. The packets position is tracked using a Cartesian coordinate system, however for ease of

¹A voxel is a 3D pixel

²all variables given in this section are the same as they are in the code.

computation for calculating scattering angles (see ??), the direction vectors are computed in a spherical system thus the direction vectors are:

$$n_{xp} = \sin(\theta) \cdot \cos(\phi) \quad (1.5)$$

$$n_{yp} = \sin(\theta) \cdot \sin(\phi) \quad (1.6)$$

$$n_{zp} = \cos(\theta) \quad (1.7)$$

θ and ϕ are generated dependant on the photon source used.

1.2.2.3 Photon move

The next step in the algorithm is moving a packet to the next interaction point. The probability a packet will interact over a distance dL is $\mu_t dL$, where μ_t is the interaction probability (see Section 1.4). Thus the probability of travelling dL without any interaction is $1 - \mu_t dL$. Therefore over a distance L , with N segments of length L/N the probability of travelling L before any interaction:

$$P(L) = (1 - \mu_t \frac{L}{N}) \cdot (1 - \mu_t \frac{L}{N}) \dots (1 - \mu_t \frac{L}{N}) = (1 - \mu_t \frac{L}{N})^N \quad (1.8)$$

$$P(L) = \lim_{N \rightarrow \infty} (1 - \mu_t \frac{L}{N})^N = e^{-\mu_t L} = e^{-\tau} \quad (1.9)$$

Where τ is the number of mean free paths over a distance L . We now have a PDF, Eq. (1.9), for the distance a packet will travel before an interaction occurs. For this to be of use we need to be able to sample from this PDF in order to get a random optical depth. Using the Monte Carlo method described in Section 1.1.1, with ξ as our random variable, we get:

$$\xi = \int_0^\tau e^{-\tau'} = 1 - e^{-\tau} \rightarrow \tau = -\log(1 - \xi) \quad (1.10)$$

As ξ is symmetric about 0.5 we can substitute $1 - \xi$ for ξ yielding:

$$\tau = -\log(\xi) \quad (1.11)$$

We now have an optical distance, however we need to convert this into a physical distance so that we can move our photon packet. From our definition of τ we know that $\tau = \int_0^L \mu_t dS$, and if we have a smooth, homogeneous medium (i.e not a gridded medium) thus

$$L = \frac{\tau}{\mu_t} \quad (1.12)$$

Therefore in order to update the packets position is simply:

$$x_p = x_p + L \cdot n_{xp} \quad (1.13)$$

$$y_p = y_p + L \cdot n_{yp} \quad (1.14)$$

$$z_p = z_p + L \cdot n_{zp} \quad (1.15)$$

However as the code in this thesis is a 3D gridded Cartesian code, we have to slightly adjust how we move and update the packets position. As stated in Section 1.2.2.1, the medium has been discretised onto a grid, so that each voxel can have a different μ_t , thus Eq. (1.12) becomes:

$$L = \frac{\tau}{\mu_{t,\zeta}} \quad \zeta = (x, y, z) \quad (1.16)$$

with $\mu_{t,\zeta}$ the μ_t for the ζ^{th} voxel. The position is then updated as before using Eqs. (1.13) to (1.15). The next step in the algorithm is the interaction event, which can consist of either: scattering, absorbing or fluorescing.

1.2.2.4 Photon scatter and absorbing

The first part of this section of the algorithm is to decide what kind of interaction the packet has with the medium. This section will focus on scattering and absorbing with other interaction events left for the chapters that detail these behaviours.

To decide whether a packet scatters or absorbs involves ‘throwing’ a random number and comparing it against the albedo. As detailed in Section 1.4 the albedo is the scattering probability $a = \frac{\mu_a}{\mu_a + \mu_s}$. The random number is compared to the albedo, and if the random number is less than the albedo then the packet scatters, otherwise the packet is absorbed.

Packet absorption

If the interaction event is a photon packet absorption, then the algorithm terminates the photon packets and starts the next photon packet, Section 1.2.2.5.

Packet scattering

If the interaction event is a packet scattering, then the packet is scattered into a new direction and the above process are carried out until a termination clause is met, see Section 1.2.2.5.

Depending of the medium being simulated, it can either be isotropically scattering or preferentially scattering in a direction. In the case of simulating photon propagation in tissue, tissue is highly forward scattering.

Anisotropy is the degree of deviation in the photon packets path at each interaction event. The measure of anisotropy is the g value, g . With g taking any value from -1 to 1 , -1 is highly backward scattering, 0 is isotropic scattering and 1 is highly forward scattering.

1.2.2.5 Termination

1.2.3 Code details

This section details the the actual implementation of the MCRT algorithm detailed in the previous section, along with any computational necessities and speed ups on the original algorithm.

1.3 Validation of MCRT code

1.4 Optical properties

1.5 Further extensions to the code

Chapter 2

Computational modelling of tissue ablation

2.1 Introduction and background

Lasers are used in wide variety of medical procedures not limited to: coagulating scalpels, port wine stain removal, tattoo removal, hair removal, and skin rejuvenation [18–22]. One class of laser used in these procedures are ablative lasers. Ablative lasers are usually high powered lasers targeted at a specific chromophore in the skin, to partially or fully remove layers of skin. These types of lasers are commonly used for aesthetic procedures such as: skin rejuvenation [22], and removal of various diseases such as Rhinophyma [23] or lesions/nodules [24]. They have also recently been investigated as a means of better drug delivery in the skin for [photo-dynamic therapy \(PDT\)](#) treatments [25].

One downside to using lasers to remove tissue, it that unlike a scalpel, where the surgeon has full control of the depth of the incision, ablative lasers are not as predictable. Lasers can also cause thermal damage to the surrounding areas, leading to unwanted effects.

Currently the only reliable method to measure the depth of the ablative holes, is via a biopsy, which is an invasive procedure. We propose to use [optical coherence tomography \(OCT\)](#) to measure the ablative crater non-invasively *in-vivo*. The [OCT](#) measurements are then backed up by a computational model. This computational model could then be used to predict the depth of the ablative crater when using a certain power for various different applications such as: laser assisted drug delivery, and various cosmetic applications.

This chapter examines using [MCRT](#) techniques coupled to a heat transfer simulation, in order to study the thermal damage to tissue due to fractional lasers. Fractionated ablative lasers are ablative lasers where the power is spread over several beams, such as to leave viable tissue around zones of damaged/necrotic tissue [26]. We present experimental work carried out on porcine tissue by our collaborators at the University of Dundee and the photobiology department at Ninewells hospital, along side our computational model of tissue ablation.

2.2 Methods

In order to replicate the experimental work *in silico*, our numerical model has three main portions. The first is the [MCRT](#) that models light transport through tissue so that we can calculate the laser energy deposited as a function of time and space. The second, a [finite difference method](#)

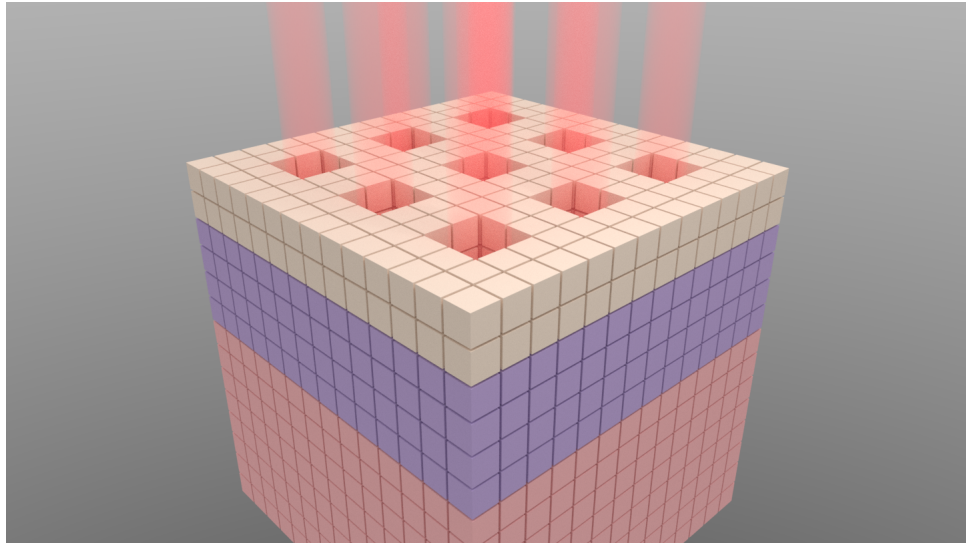


Figure 2.1: Example of a possible voxel model, with three different layers, various holes due to ablative pixel beam lasers. Each voxel can represent a different optical/thermal property of the tissue medium.

(FDM) which is used to calculate the heat diffusion within the tissue due to the absorbed laser energy. Finally, a tissue damage model to track the damage to the tissue caused by the laser. All these individual portions are connected together to create our numerical model. Each portion of the numerical model is described below in more detail.

2.2.1 Monte Carlo radiation transport (MCRT)

This part is here as it will be needed for paper. probably not needed in chapter though... **MCRT** is the ‘gold standard’ for simulating the transport of light through biological tissue [27]. This is due to its flexibility in modelling non standard geometries, and its ability to model various light sources and micro-physics, such as fluorescence. It uses interaction probabilities and random numbers in order to model the ‘random walk’ that photons undergo in a turbid medium. These ‘packets’ can undergo go scattering, absorption and various other physical process [28, 29]. **MCRT** has been used to model light-tissue interactions in many different medical and biophotonic applications [30–32]. **MCRT** is used here to calculate the energy deposited by the laser, which is then passed to the heat transport simulation.

The tissue medium for the **MCRT** and heat transport simulations is a 3D voxel model (Fig. 2.1). This allows the variation of optical and thermal properties from voxel to voxel, making it the ideal type of grid for modelling tissue ablation. We use $240 \times 240 \times 240$ voxels, representing a tissue sample size of $1.1 \times 1.1 \times 0.5$ cm. We assume the porcine skin is uniform, so initially our voxel model is uniform, and the optical properties of porcine skin at the wavelength of interest is mainly that of water mixed with protein, see Fig. 2.10.

The original **MCRT** code was developed for astronomy applications [15, 33], and has since been adapted for medical applications [30, 34].

Figure 2.2. shows the overall algorithm for the simulation, including the **MCRT** portion. The **MCRT** portion of the algorithm begins with determining where the photon enters the medium. This is calculated by randomly selecting one of the pixel beams, from the 9×9 array of pixel

beams. Next the position on the surface of the medium is calculated. As the exact profile of the pixel beams are unknown, they are assumed to be uniformly circular. Thus, the packets position is uniformly sampled on a circle the width of the pixel beam.

Once the packet enters the simulation, a propagation distance for the packet is calculated using Eq. (2.1). The packet then moves this distance before undergoing an interaction event. This can be either scattering or absorption, however in this simulation absorption dominates, and thus we assume no scattering takes place. This process is repeated until the photon has either been absorbed or exits the medium.

$$L = -\frac{\ln(\xi)}{\mu_a} \quad (2.1)$$

Where:

- ξ a random number ($\tau = -\ln(\xi)$, τ is the optical depth);
- μ_a is the absorption coefficient;
- L is the physical distance.

Equation (2.1) is the equation for a uniform medium. As the medium we are simulating changes over time due to thermal damage this equation has to be adapted for a 3D Cartesian grid. Each voxel can have different optical properties, thus the photon packet is moved on a voxel by voxel basis. To start the movement process, a random number is generated, which is used to sample an optical depth the photon packet will travel. Next the photon enters the voxel and the maximum distance the photon can travel in the new voxel is calculated along the photons trajectory. If this optical distance is less than the optical depth sampled, then the photon enters the next voxel. If the distance is larger than the sampled optical distance then the photon has an interaction event in that voxel. The photon packet moves to the interaction event in the voxel and then undergoes scattering or absorption. The whole process is repeated until the photon ‘dies’ via absorption or leaving the medium. This in turn is again repeated for all the photons, until all the photons have been absorbed or have escaped the tissue medium. We use 1 million photon packets per MCRT simulation run.

To calculate the energy absorbed in the porcine tissue via the laser we use the path length counter method devised by Lucy [35] (see Fig. 2.3). The energy absorbed per voxel is therefore calculated as:

$$E_i^{abs} = \frac{L}{N\Delta V_i} \sum \mu_{a,i}s \quad (2.2)$$

Where:

- L is luminosity [W];
- N is the number of photons;
- ΔV_i is the volume of the i^{th} voxel [m^{-3}];
- $\mu_{a,i}$ is the absorption coefficient of the i^{th} voxel [cm^{-1}];
- and s is the pathlength of a photon packet through the i^{th} voxel [cm].

This grid of absorbed energy is then passed to the heat transport portion of the simulation, so that the heat diffusion in the porcine tissue can be calculated.

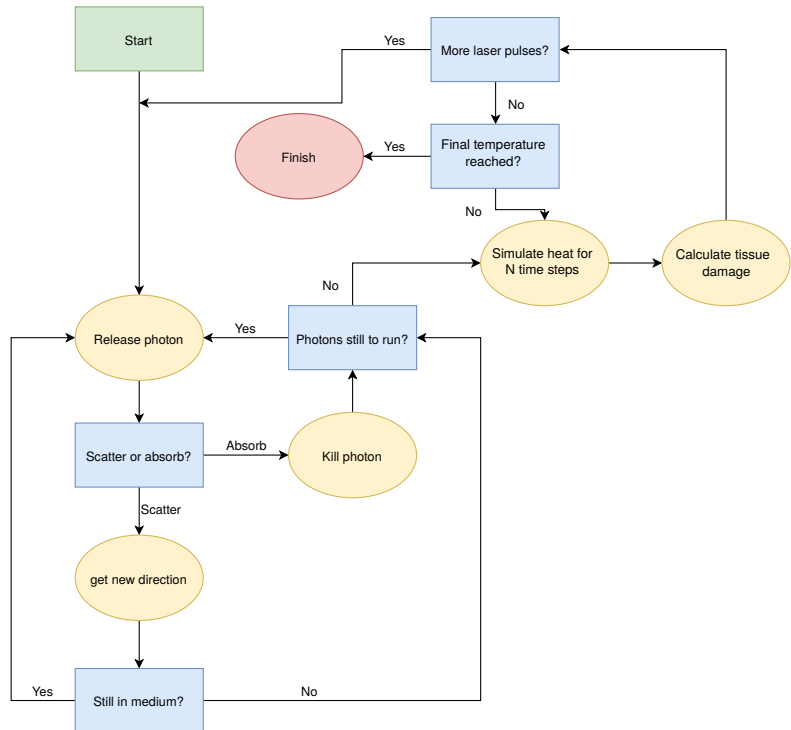


Figure 2.2: Flowchart of the tissue ablation algorithm.

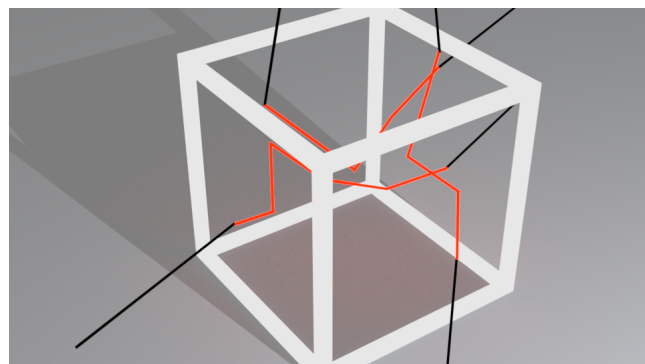


Figure 2.3: Red lines are photon paths within a voxel. Black lines photon paths outwith the voxel. Red photon paths are summed up in order to calculate the absorbed energy within each voxel.

2.2.2 Heat transport

In order to model the transport of heat in porcine skin, we use the standard parabolic heat equation:

$$\rho c_p \frac{\partial T}{\partial t} = \nabla \cdot (\kappa \nabla T) + \dot{q} \quad (2.3)$$

Where:

- $T(x, y, z, t)$ is the temperature as a function of time and space [K];
- κ is the thermal conductivity [$W \cdot m^{-1} \cdot K^{-1}$];
- ρ is the density [$Kg \cdot m^{-3}$];
- c_p the specific heat capacity [$J \cdot K^{-1}$];
- $\dot{q}(x, y, z, t)$ is the source/sink term as a function of time and space [$W \cdot m^{-3}$].

As we are modelling a dynamic system, where the tissue's optical and thermal properties change as a function of space and time, we cannot make the assumption that κ , ρ , and c_p are constant and thus we have to solve the non-linear heat equation (Eq. (2.4)).

$$\frac{\partial T}{\partial t} = \frac{1}{(\rho c_p)_\xi} (\nabla k_\xi T + k_\xi \nabla^2 T) + \dot{q} \quad \xi = (i, j, k) \quad (2.4)$$

The \dot{q} term is a heat source/sink term. The heat source in this simulation is due to the laser, and we assume the only loss of heat to the surrounding medium is via convection and conduction.

These boundary conditions must be considered. All faces of the cube, bar the laser facing face, are considered to be pinned at $5^\circ C$, as the porcine skin was kept cooled prior to experimental work and the simulation volume is smaller than the porcine tissue samples. The laser facing face has a simple convective BC:

$$\dot{q}_c = -hA(T - T_\infty) \quad (2.5)$$

Where:

- h is the heat transfer coefficient [$W \cdot m^{-2} \cdot K$];
- A is the area of the grid element, that is radiating/convicting heat away [m^{-2}];
- and T , and T_∞ are the temperature in a voxel and the surrounding medium temperature respectively [K].

As Eq. (2.4) is generally hard to solve in arbitrary geometries with complex boundary conditions we employ a numerical method to solve Eq. (2.4). The numerical method we employ is a **FDM**. The FDM is derived from the Taylor series approximation for derivatives. A function $f(x)$ is discretised onto a grid with N nodes (see Fig. 2.4). Then at a node i we can use the Taylor series approximation in the forward (+ive x direction) and backward (-ive x direction) to give the derivates in Eqs. (2.6a) and (2.6b). Where: i is the grid point at x_o , $i+1$ is the point at $x_o + \Delta x$, and $i-1$ is the grid point at $x_o - \Delta x$. We can then combine these 'forward' and 'backward' derivatives to give a 'central' derivative Eq. (2.6c). We can also give expressions for the 2^{nd} order derivatives for backward, forward and central (forward and backward 2^{nd} order equations omitted for brevity) Eq. (2.6d).

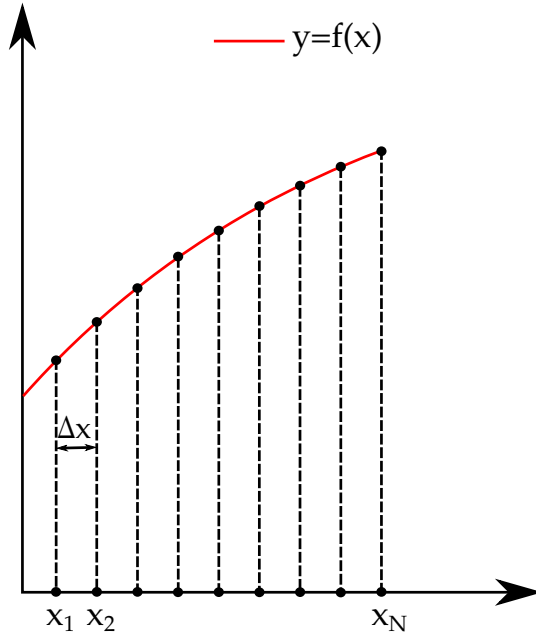


Figure 2.4: Discretisation of $f(x)$.

$$\frac{df}{dx} = \frac{f_{i+1} - f_i}{\Delta x} \quad (\text{forward}) \quad (2.6a)$$

$$\frac{df}{dx} = \frac{f_i - f_{i-1}}{\Delta x} \quad (\text{backward}) \quad (2.6b)$$

$$\frac{df}{dx} = \frac{f_{i+1} - f_{i-1}}{2\Delta x} \quad (\text{central}) \quad (2.6c)$$

$$\frac{d^2f}{dx^2} = \frac{f_{i-1} - 2f_i + f_{i+1}}{\Delta x^2} \quad (\text{central}) \quad (2.6d)$$

Thus the linear heat equation Eq. (2.3), in 1D, taking a 1^{st} order forward time derivative, and a 2^{nd} order central spatial derivative gives:

$$\frac{T_i^{n+1} - T_i^n}{\Delta t} = \alpha \frac{T_{i-1}^n - T_i^n + T_{i+1}^n}{\Delta x^2} + \frac{\dot{q}}{\rho c_p} \quad (2.7a)$$

$$T_i^{n+1} = \alpha \Delta t \frac{T_{i-1}^n - 2T_i^n + T_{i+1}^n}{\Delta x^2} + \frac{\dot{q}}{\rho c_p} \quad (2.7b)$$

Equation (2.7b) is called the ‘simple explicit form of finite-difference approximation’ [36]. Figure 2.5 shows the ‘stencil’ of this scheme, where there are three known points at time N , and just one unknown at time $N+1$. There are various other scheme that can be used to calculate the temperature at the the next time step. However we use a simple explicit scheme here, due to its ease of implementation despite its stability being constrained in comparison to an implicit method. This method is also easily scaled up to 3D with little difficulty.

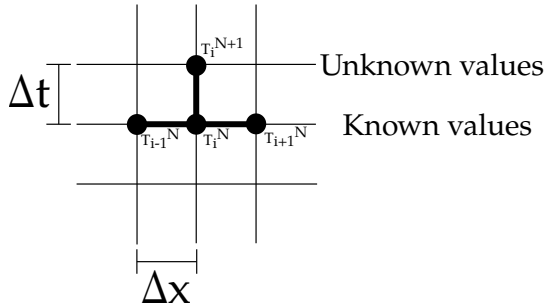


Figure 2.5: Finite difference method stencil for simple explicit scheme

For the more complicated non-linear heat equation we have to account for the change of the medium between points in the space and time. The two easiest methods [36] of achieving this is: One, lag the value behind by one step, i.e $c_p^{n+1} = c_p^n$. Two, average κ , ρ , and c_p using a half difference scheme:

$$\kappa^\pm = \frac{\kappa_i + \kappa_{i\pm 1}}{2} \quad (2.8)$$

$$\rho^\pm = \frac{\rho_i + \rho_{i\pm 1}}{2} \quad (2.9)$$

$$c_p^\pm = \frac{c_{p,i} + c_{p,i\pm 1}}{2} \quad (2.10)$$

Thus for the simple 1D case as in Eq. (2.7b), we average the thermal properties when computing the coefficients of the temperature nodes, and lag the thermal properties when adding the heat from the laser:

$$T^{N+1} = \Delta t (AT_{i-1}^N - 2BT_i^N + DT_{i+1}^N) + T_i^N + \frac{\dot{q}_L}{\rho c_p} \quad (2.11)$$

Where:

$$\begin{aligned} A &= \frac{\kappa^-}{\rho^- c_p^- 2\Delta x^2} \\ B &= \frac{\kappa^+}{\rho^+ c_p^+ 2\Delta x^2} \\ D &= \frac{(A+B)}{2} \end{aligned} \quad (2.12)$$

Equation (2.11) can be generalised to higher dimensions easily. The 3D case gives:

$$U_{xx} = (AT_{i-1,j,k}^N - 2BT_{i,j,k}^N + DT_{i+1,j,k}^N) \quad (2.13)$$

$$U_{yy} = (AT_{i,j-1,k}^N - 2BT_{i,j,k}^N + DT_{i,j+1,k}^N) \quad (2.14)$$

$$U_{zz} = (AT_{i,j,k-1}^N - 2BT_{i,j,k}^N + DT_{i,j,k+1}^N) \quad (2.15)$$

$$T_{i,j,k}^{N+1} = \Delta t (U_{xx} + U_{yy} + U_{zz}) + T_{i,j,k}^N + \frac{\Delta t}{\rho c_p} \dot{q}_L \quad (2.16)$$

Where:

- $T_{i,j,k}^{N+1}$ is the new temperature at node i, j, k [K];
- $T_{i,j,k}^N$ is the temperature at node i, j, k at the current time step [K];
- α is the thermal diffusivity [$m^2 \cdot s^{-1}$];
- κ is the thermal conductivity [$W/m \cdot K$];
- Δx etc. is the size of the grid element in the p^{th} direction [m];
- and A, B, D are the coefficients in their respective dimension (Eq. (2.12)).

Incorporating B.Cs on the top air exposed face:

$$U_{zz} = \frac{\alpha}{\Delta z^2} \left(\frac{2\Delta z}{\kappa} (-h(T_{i,j,k}^N - T_\infty^N)) - 2T_{i,j,k}^N + 2T_{i,j,k+1}^N \right) \quad (2.17)$$

Equations (2.16) and (2.17) give the full numerical solution to the non-linear heat equation with a convection boundary term and laser heat source. This will allow us to calculate the heat diffusion in the porcine tissue due to laser heating.

As the lasers operate in a pulsed mode, we account for this in our simulation. We assume that the pulse shape is a top-hat pulse for simplicity. In the heat simulation we have an additional variable in the term $laserOn \cdot \frac{\alpha \Delta t}{\kappa} q_L$ in Eq. (2.16). This additional variable, $laserOn$, is a boolean value, which is defined as:

$$laserOn = \begin{cases} 1, & \text{Laser on} \\ 0, & \text{Laser off.} \end{cases}$$

In the instance where there is more than one pulse, the laser is turned on and off based upon the pulse frequency.

As we are using a simple explicit FDM, the time step is constrained in order to make the solution stable. For a cubic 3D FDM without prescribed flux BCs, yields the constraint: $\Delta t \leq \frac{1}{\delta \alpha}$ where $\delta = \frac{1}{\Delta x^2} + \frac{1}{\Delta y^2} + \frac{1}{\Delta z^2}$. However as we have a convection prescribed boundary condition, the constraint on the time is more severe. Along with this time restraint, the pulse length of the laser also has to be considered. If the time step of the heat simulation is too large it will not account for the heat deposited by the laser. Thus, the timestep has to be an order of magnitude smaller than the shortest laser pulse.

As the timestep is small, and the grid resolution large, the resultant simulation is slow. Thus the code has been fully parallelised to improve performance. Both the MCRT and heat simulation are independently parallelised. As discussed in Chapter 1, the MCRT simulation is fully parallelised, and the results are passed to the heat simulation.

Parallelisation of the heat simulation is more involved than the ‘embarrassingly parallel’ class of problems that MCRT belongs to. This is due to the heat simulation being dependant on the temperature of adjacent nodes. Thus information will have to be passed from each individual core during computation, as opposed to doing the information passing at the end of the simulation à la MCRT parallelisation. The heat simulation is parallelised using a technique called ‘halo swapping’. This involves splitting up the computational domain (see Fig. 2.6), in this case the tissue medium, and doing the calculations on each domain on a separate core. The ‘halo swapping’ comes in when cores need to communicate with each other about updating their boundary temperature nodes (see Fig. 2.7).

On a workstation computer these simulations were carried out on (Intel Xeon E3-1245 v5, 8 core @ 3.5GHz) led to a speed up of ~6, over the serial simulation. Using Amdahl’s law [37], the serial portion of the simulation is ~ 5%, giving a theoretical speed up ~ 20 times the serial simulation.

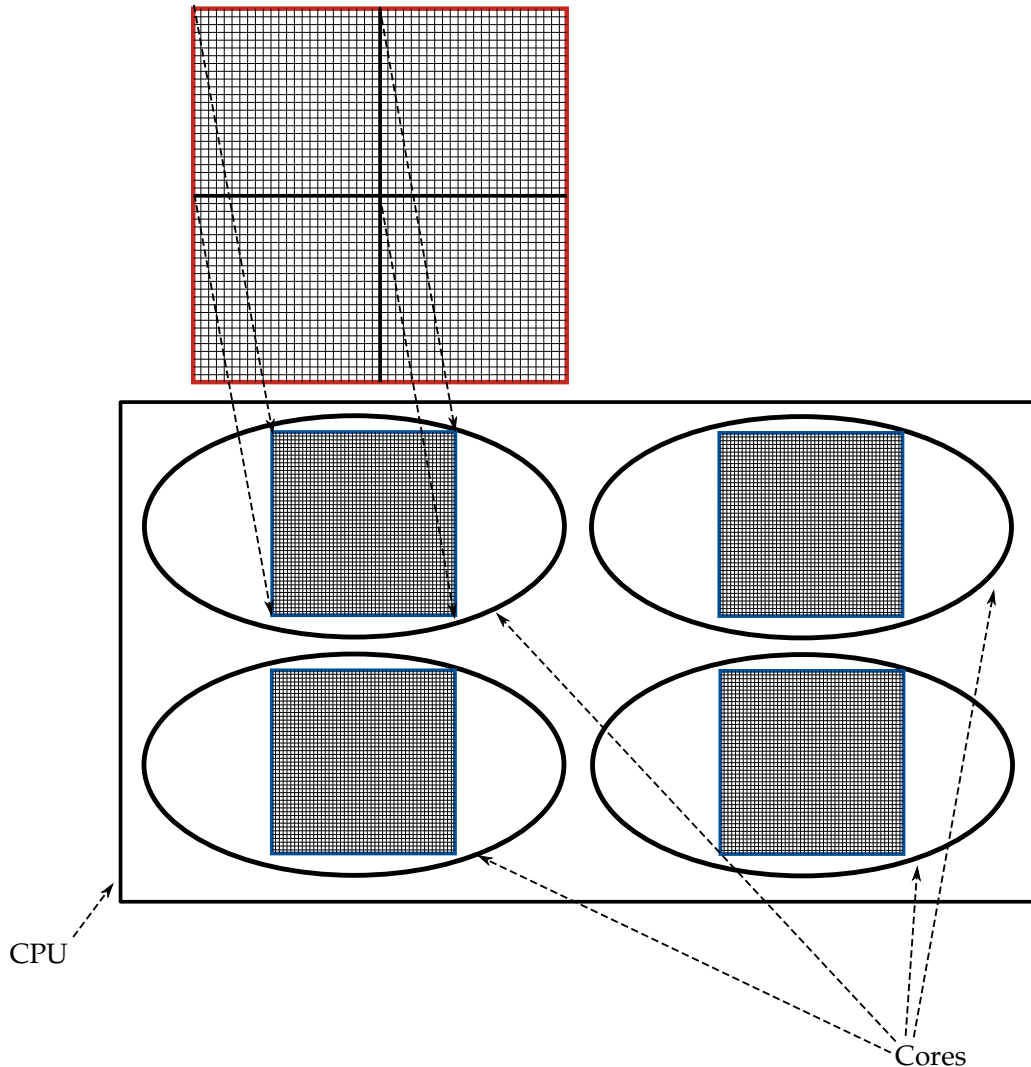


Figure 2.6: Computational domain decomposition. Total computational domain (red outline) is evenly divided between cores in the CPU. This is done via layers of the domain in the z direction. Information is passed to/from cores via the ‘halo swap’ process (see Fig. 2.7).

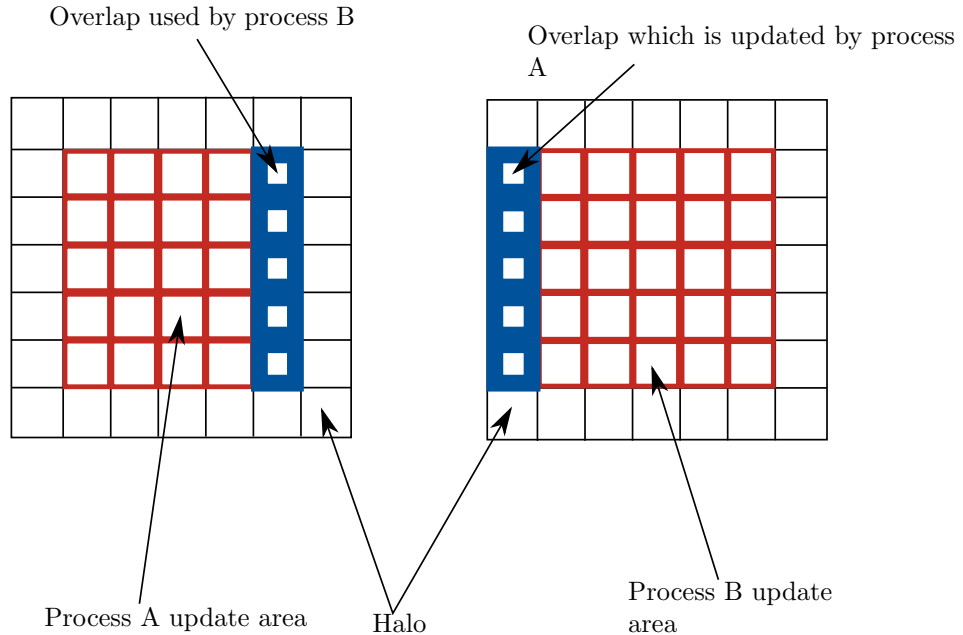


Figure 2.7: Halo swapping. Process A updates the area in red and blue on the left. It updates the blue area which is sent to process B as B's 'halo'. Process B cannot update its own halo, but rather updates the halo for process A.

After the heat transport has been completed, the grid of temperatures is passed to the tissue damage portion of the simulation.

2.2.3 Tissue Damage

2.2.3.1 Introduction

The final portion of the simulation is the tissue damage model. To be able to model damage to the tissue we first need to be able to describe the tissue damage process due to heating from a laser.

When the laser is turned on, the temperature starts to rise within the tissue due to the absorption of photons by the tissue. The temperature rise causes damage to the tissue when above a threshold temperature, T_d , approximately 43°C [1]*p539*. From the temperature, T_d , we define four main areas of tissue damage:

$$T = \begin{cases} \text{coagulation,} & T_d \leq T \leq 100 \\ \text{water boils,} & T = 100 \\ \text{carbonisation,} & 100 \leq T \leq T_a \\ \text{ablation,} & T = T_a. \end{cases} \quad (2.18)$$

The area of tissue damage we term 'coagulation' is a multifaceted process. At 43°C - 50°C , bonds break within cell membranes, causing ruptures, and some cell death [1]. This process is usually termed *hyperthermia*. Around 50°C , enzyme activity decreases, cells become immobile, and various cell repair mechanisms are disabled, leading to more cell death. Temperatures of 60°C +, proteins become denatured. Thermal denaturation is a structural and functional change

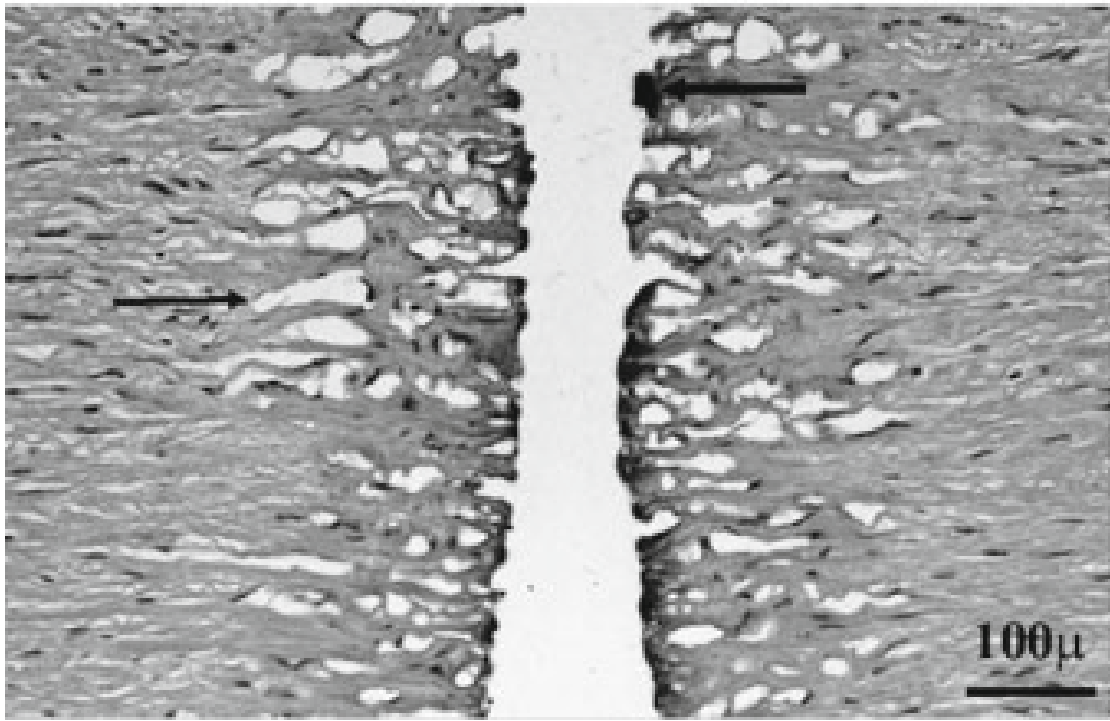


Figure 2.8: Tissue ablations, as viewed under a microscope. Steam vacuoles are clearly visible either side of the ablation area. Carbonisation is also evident at the edges of the ablation fronts. Adapted from [1].

in a protein due to the heating it undergoes. This means they change from a highly organised structure with specific purposes, to disorganised structures with no function at all. A classic example of denaturation of proteins, is in cooking eggs. Denaturation occurs when the clear fluid egg white, rich in protein albumin, becomes a solid white [38].

The next stage in the tissue damage process is the vaporisation of water. As the temperature of the tissue starts to approach 100°C (at 1 atm), water starts to vaporise. If the vaporised water cannot escape the tissue it forms steam vacuoles, little pockets of steam. These vacuoles can easily been seen when viewing tissue samples after tissue has been treated with a high powered laser (see Fig. 2.8). In certain conditions these steam pockets can explode, with these ‘explosions’ being audible by the human ear [39].

The third stage of tissue damage is carbonisation or caramellisation of the tissue. This occurs when most of the water has boiled off, leaving the remaining tissue to heat up and reduce to its elemental carbon form. This carbonisation of tissue, when it occurs, is generally only a thin layer of $5\text{-}20 \mu\text{m}$ [1].

The final stage of tissue damage is the removal of the remaining tissue, i.e tissue ablation. There is no agreement in the literature how tissue undergoes ablation with a number of methods proposed [40]. The tissue ablation process is not a simple process, with various unknowns which depend on everything from tissue composition to laser power and pulse length. The literature however, does suggest that it takes place when the tissue temperature is between 177 and 500°C [41, 42].

In order to model all these tissue damage processes we split our tissue damage model into two sections: ‘physical’ damage and coagulation damage. Where ‘physical’ damage changes the tissue optical and thermal properties, where the coagulation damage has no effect on the tissue’s

optical or thermal properties.

2.2.3.2 Modelling coagulation damage

With the description of the various process that tissue undergoes during ablation, we can now create a numerical model of these processes. First, in order to model the full extent of the damage done under 100°C, i.e in the coagulation regime, we use the Arrhenius damage model. The Arrhenius damage model was originally used as a kinetic model of reaction products in chemistry [43]. It has since been adapted by various authors for modelling tissue damage [44,45]. These authors and various others, adapted this model by fitting Eq. (2.19) to experimental data for burn damage. The two parameters fitted in this way are the A, the frequency factor, and ΔE , the activation energy.

$$\Omega(t) = \int_{t_i}^{t_f} Ae^{-\frac{\Delta E}{RT}} d\tau \quad (2.19)$$

Where:

- Ω is the damage value;
- A is ‘frequency factor’ [s^{-1}];
- ΔE is activation energy [$J \cdot mol^{-1}$];
- R is the universal gas constant [$J \cdot mol^{-1} \cdot K^{-1}$];
- T is the temperature [K];
- and t_i and t_f are the initial time and final time at t_{crit} .

It is reported that a value of Ω of 0.53, 1.0, and 10^4 relate to first, second, and third degree burns respectively [46]. We use the Arrhenius damage model in order to better understand the amount of damage caused by the laser in the non-ablated areas of tissue. This can give us an insight into the various physical phenomena encountered in the OCT results.

2.2.3.3 Modelling physical tissue damage

As tissue mostly consists of water *ref* when the temperature of the tissue approaches 100°C (at 1 atm), water in the tissue begins to boil off. This acts as a large heat sink for the absorbed laser energy, slowing down the rate of ablation. The energy required to boil the water is $Q_{vapor} = m_v \cdot L$, where m_v is the mass of a voxel, and L is the latent heat of vaporisation. The energy to boil off the water is provided via the laser and heat diffusing into the voxel:

$$Q_{vapor} = \underbrace{laserOn \cdot \dot{q} \cdot \Delta t \cdot V_{i,j,k}}_{\text{laser heating}} + \underbrace{c \cdot M_{i,j,k} \cdot \Delta T}_{\text{heat diffusion}} \quad (2.20)$$

Where:

- Q_{vapor} is the current energy in Joules that has been used to boil off the water in the voxel [J];
- $laserOn$ is a boolean variable that determine if the laser is on or off [-];
- \dot{q} is the energy absorbed by the voxel due to the laser [$W \cdot m^{-3}$];
- Δt is the timestep [s];
- $V_{i,j,k}$ is the volume of the i^{th} , j^{th} , k^{th} voxel [m^3];
- c is the heat capacity of the voxel [$J \cdot K^{-1}$];
- $M_{i,j,k}$ is the mass of the i^{th} , j^{th} , k^{th} voxel [Kg];
- and ΔT is the change in temperature the voxel would undergo, if the water was not boiling off.

As water boils off, the water content of each voxel changes. This affects the absorption coefficient, density, thermal conductivity, and heat capacity. Each of these vary linearly with water content per voxel [47];

$$W = W_{init} - \left(W_{init} \cdot \left(\frac{Q_{current}}{Q_{vaporisation}} \right) \right) \quad (2.21)$$

$$\rho = \frac{1000}{W + 0.649 \cdot P} \quad (2.22)$$

$$c_p = 4.2 \cdot 10^3 \cdot W + 1.09 \cdot 10^3 \cdot P \quad (2.23)$$

$$\kappa = \rho \cdot (6.28 \cdot 10^{-4} \cdot W + 1.17 \cdot 10^{-4} \cdot P) \quad (2.24)$$

$$\mu_a = W \cdot \mu_{water} + \mu_{protein} \quad (2.25)$$

$$(2.26)$$

Where:

W is the water content (i.e $W = 0.7$ equates to 70% water content);

W_{init} is the initial water content;

$Q_{current}$ is the total energy absorbed by the i^{th} voxel since the temperature reached 100°C [J];

P is the protein content (i.e $P = 1.0 - W$);

κ is the Thermal conductivity [$W \cdot m^{-1} \cdot K^{-1}$];

c_p is the heat capacity [$J \cdot Kg^{-1} \cdot K^{-1}$];

and μ_a is the total absorption coefficient, and μ_{water} and $\mu_{protein}$ are the absorption coefficients of water and protein respectively.

We define the T_a as occurring between 177 and 500°C [41, 42]. At T_a the tissue is removed and the thermal, optical, and physical properties set to that of air.

The updated damaged tissue structure is then fed back to the MCRT model and the whole process repeats until the predefined time limit is reached. This whole process of photon propagation, heat diffusion and tissue damage is outlined in Fig. 2.2.

2.2.4 Validation

2.2.4.1 Heat transport validation

In order to thoroughly validate the numerical method we employ to solve the heat equation, we compare the numerical method against an easily solvable case. We solve the heat equation on a cube, side L, in a surrounding medium of 0°C. The cube is initially at temperature 37°C and we calculate the temperature at time $t=0.1s$. Thus the boundary conditions are:

$$T(0, y, z, t) = T(x, 0, z, t) = T(x, y, 0, t) = 0^\circ C \quad (2.27)$$

$$T(L, y, z, t) = T(x, L, z, t) = T(x, y, L, t) = 0^\circ C \quad (2.28)$$

$$(2.29)$$

The thermal diffusivity (α), density (ρ), and heat capacity (c_p) are all set to 1. Assuming a separable solution in Cartesian coordinates for the heat equation yields:

$$\begin{aligned} T(x, y, z, t) = & (A_1 \cos(\alpha x) + A_1 \sin(\alpha x)) \cdot \\ & (B_1 \cos(\beta y) + B_1 \sin(\beta y)) \cdot \\ & (C_1 \cos(\gamma z) + C_1 \sin(\gamma z)) \cdot e^{-\alpha \mu^2 t} \end{aligned} \quad (2.30)$$

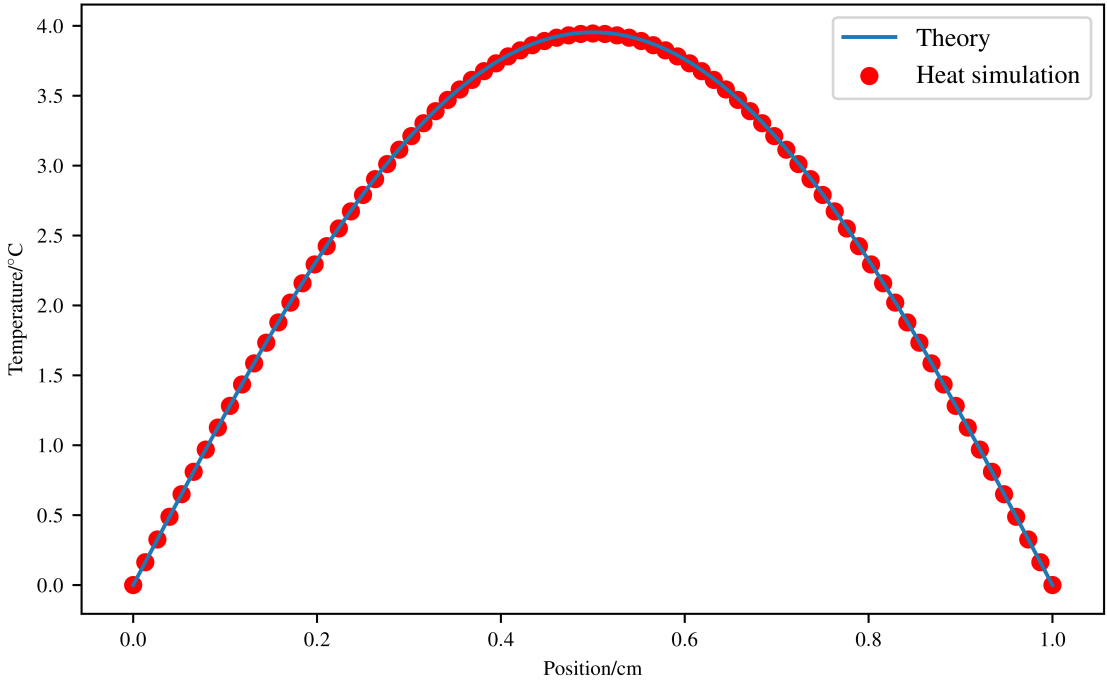


Figure 2.9: Comparison between analytical solution and numerical method.

$$\mu^2 = \alpha^2 + \beta^2 + \gamma^2 \quad (2.31)$$

Applying the boundary conditions (Eqs. (2.27) and (2.28)) gives:

$$A_1 = B_1 = C_1 = 0 \text{ and } \alpha = \frac{\pi n}{L}, \beta = \frac{\pi m}{L}, \gamma = \frac{\pi p}{L} \quad (2.32)$$

$$\therefore T_{nmp}(x, y, z, t) = A_{nmp} \sin\left(\frac{\pi n x}{L}\right) \cdot \sin\left(\frac{\pi m y}{L}\right) \cdot \sin\left(\frac{\pi p z}{L}\right) \quad (2.33)$$

This yields the following solution for the heat equation using the principle of superposition, and solving Eq. (2.34) with $f(x, y, z)$ as the initial temperature profile of the cube:

$$A_{nmp} = \frac{8}{L^3} \int_0^L \int_0^L \int_0^L f(x, y, z) \cdot \sin\left(\frac{\pi n x}{L}\right) \cdot \sin\left(\frac{\pi m y}{L}\right) \cdot \sin\left(\frac{\pi p z}{L}\right) dx \cdot dy \cdot dz \quad (2.34)$$

$$T(x, y, z, t) = \sum_{n=1,3,\dots}^{\infty} \sum_{m=1,3,\dots}^{\infty} \sum_{p=1,3,\dots}^{\infty} \frac{2368}{\pi^3 nmp} \sin\left(\frac{\pi n x}{L}\right) \sin\left(\frac{\pi m y}{L}\right) \sin\left(\frac{\pi p z}{L}\right) e^{(-\lambda^2 t)} \quad (2.35)$$

Where:

$$\lambda^2 = \alpha\pi^2\left(\frac{n^2}{L^2} + \frac{m^2}{L^2} + \frac{p^2}{L^2}\right);$$

n, m, p are odd integers;

and L is the length of the cube.

At time, $t = 0.1\text{s}$, a slice through the middle of the cube, $L = 1\text{ cm}$, yields Fig. 2.9.

2.2.4.2 MCRT & heat transport validation

As a first test of our code, both MCRT and heat simulation, we compare to a simple analytical model of ablation. The simple model of ablation is as this: We define the ablation energy (E_a) as the minimum energy required to raise the temperature of the medium to 100 °C, and then boil off the water in a volume dV , mass M . Thus in 1 dimension we have Eq. (2.36), where the symbols have their usual meanings. If the energy for ablation is delivered in a time dt by a laser of power density ($W\text{cm}^{-2}$) this gives Eq. (2.37). Equation (2.37) can be rearranged in order to give an ablation front velocity, Eq. (2.38).

$$E_a = c_p \rho dx \Delta T + L_v \rho dx \quad (2.36)$$

$$P \cdot dt = \rho dx (c_p \Delta T + L_v) \quad (2.37)$$

$$u = \frac{P}{\rho (c_p \Delta T + L_v)} \quad (2.38)$$

Assuming the ablation front moves with constant velocity during the ablation, and using $L_v = 2.53 \cdot 10^6 \text{ J} \cdot \text{Kg}^{-1}$, $c_p = 4181 \text{ J} \cdot \text{Kg}^{-1} \cdot \text{K}^{-1}$ and the medium is a cube side 2 mm, with a starting temperature is 37 °C with a water content of 70% giving a density of $700 \text{ Kg} \cdot \text{m}^{-3}$. For these parameter this gives an ablation velocity, $u \simeq 0.77 \text{ cm} \cdot \text{s}^{-1}$, and a time to ablate through 2 mm of $t \simeq 0.26 \text{ s}$. As the code developed in this chapter simulates the diffusion of heat in a medium due to an incident laser, the expected time to ablate through the same medium should be slightly less as heat diffuses away from the voxel while it is heated being heated. When the full heat + MCRT code is used to simulate this experiment, it gives a time, $t \simeq 0.33 \text{ s}$.

maybe more? Could compare to <https://doi.org/10.11117/1.2204615>. They use MCRT + FDM but no ablation. So would be good test

2.3 *In silico* results

2.3.1 Introduction

In order to match the experimental results, we must first create as accurate model of the experimental setup *in silico*. However due to computational constraints, such as memory and time available, we must make some approximations to the experimental setup. The porcine skin was a large thin slice of the top most layers of the skin. However as the area of interest is where the ablation occurs, we initially model the porcine skin as a cuboid, dimensions: $1.1 \times 1.1 \times 0.5 \text{ cm}$. The initial temperature of the porcine skin is assumed to be around 5°, as the tissue was kept on ice or was kept cooled. As mentioned in the previous sections, there are several unknowns in the model: T_a , water content, temperature of air after ablation, and the exact thermal and optical properties of the porcine tissue. Therefore we run several models so that the full parameter space of these unknowns can be explored. Results from these *in silico* experiments are presented in this section along with a comparison of the model to the experimental work carried out in collaboration with the University of Dundee and the photobiology department at Ninewells hospital.

2.3.1.1 Optical & thermal properties

As mentioned, the thermal and optical properties of porcine tissue are not known exactly for a given tissue sample. This is due to no one tissue sample being exactly the same as another

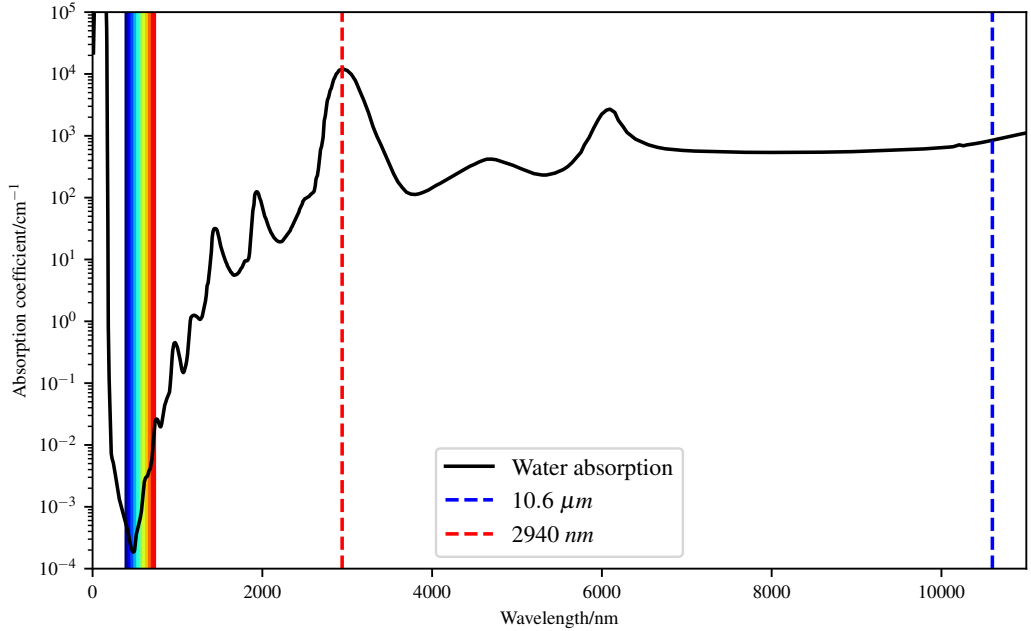


Figure 2.10: Water absorption coefficient for wavelengths 0-12000nm [2]. Data shows that water is highly absorbing in the infra-red portion of the spectrum compared to the visible portion.

	Thermal conductivity, κ	Density, ρ	Heat capacity, c
Tissue	$\rho \cdot (6.28 \cdot 10^{-4} \cdot W + 1.17 \cdot 10^{-4} \cdot P)$	$\frac{1000}{W+0.649 \cdot P}$	$4.2 \cdot 10^3 \cdot W + 1.09 \cdot 10^3 \cdot P$
Air	$a e^{-b(T-273.15)} + c$	$\frac{p_{atm}}{R_{spec}T}$	1006

Table 2.1: Optical and thermal properties for porcine tissue and air in SI.

sample, due to various factors. As such the thermal and optical properties used in this section are taken from various literature source and are modified over a range that is deemed acceptable according to various sources.

Both of the lasers used in the experimental work are infrared lasers, this means that the optical properties of the tissue are dominated by water absorption (see Fig. 2.10). The lasers used in the experiment are the Lynton lumina 576 Er:YAG, and the Pixel CO₂. The Er:YAG laser has a wavelength 2940 nm which corresponds to an absorption coefficient of water: $\sim 11200 \text{ cm}^{-1}$. The CO₂ laser has a wavelength 10.6 μm which corresponds to an absorption coefficient of $\sim 850 \text{ cm}^{-1}$. As the absorption coefficient is large, we assume that scattering is negligible at these wavelengths. Table 2.1 summarises the thermal properties for tissue and air used in the simulations.

Both lasers were used in ‘Pixel beam’ mode. This means that the laser beam is split into an array of smaller beams. The Er:YAG laser used a pattern of 5 x 5 lasers, with the corners missing, giving a total of 21 ‘Pixel beams’. The CO₂ laser used an array of 81 pixel beams with no missing ‘Pixels’. As the CO₂ laser was upgraded during the period in which the experimental data was taken, we present both sets of data, pre-upgrade and post-upgrade. The upgrade consisted of an update to the laser power, from 30 W to 70 W.

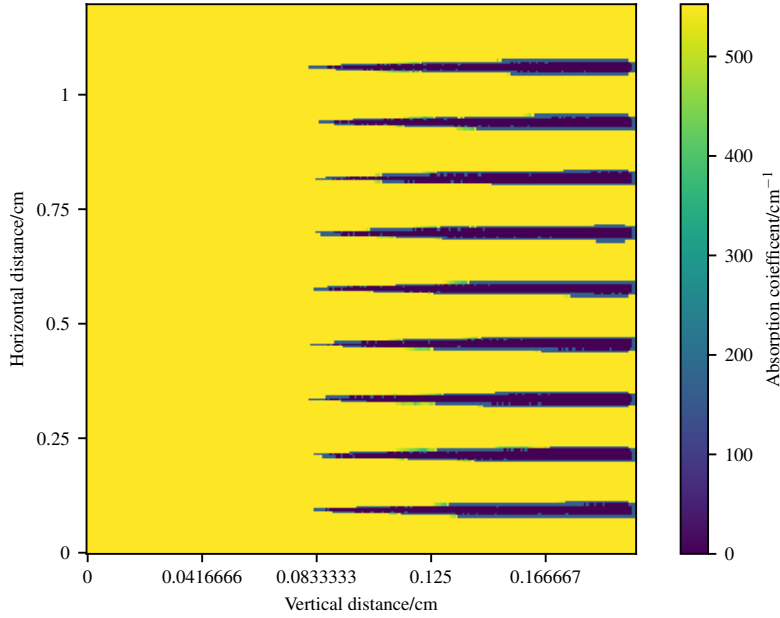


Figure 2.11: Simulation of 81 pixel beams. Figure is a slice through the optical properties at the end of the simulation. Yellow is unchanged tissue, and purple is completely ablated tissue. Figure shows that the ablation craters do not overlap one another.

Both lasers operated in different modes; the Er:YAG delivered multiple pulses of either 350 mJ or 700 mJ, and the CO₂ delivered one single pulse of varying energy over the range 50 mJ to 400 mJ. The experiment consisted of ablating the porcine tissue, as a function of energy per ‘pixel’ beam. This was achieved by either stacking multiple pulses on top of each other for the Er:YAG laser over a range of 350 mJ to 3500 mJ. For the CO₂ the pulse length of each pulse was adjusted, so that the energy per pulse was varied over a range 50 mJ to 400 mJ. The energy range for the CO₂ laser was kept the same pre and post-upgrade.

2.3.1.2 Computational speed up:

As mentioned in the introduction, the volume of interest is the area around the ablation craters. The volume is $1.1 \times 1.1 \times 0.5 \text{ cm}$. However, in order for the simulation to have good resolution of the ablation craters, this volume would require a large number of voxels for the tissue model. This is unfeasible due to: the memory required to store the various counters, and variables, and the time that would be required in order to carry out the computation. Thus the volume of interest is reduced to focus on just one of the ablation craters that is created by the laser. As a sanity check to ensure that we are not omitting any phenomena by focusing on just one ablation crater, an initial simulation that simulates the full volume of interest was carried out to investigate the possibility of overlapping craters or other related phenomena. The simulation, as shown in Fig. 2.11, gives us validation that the shrinking of the volume of interest is a valid approximation to make.

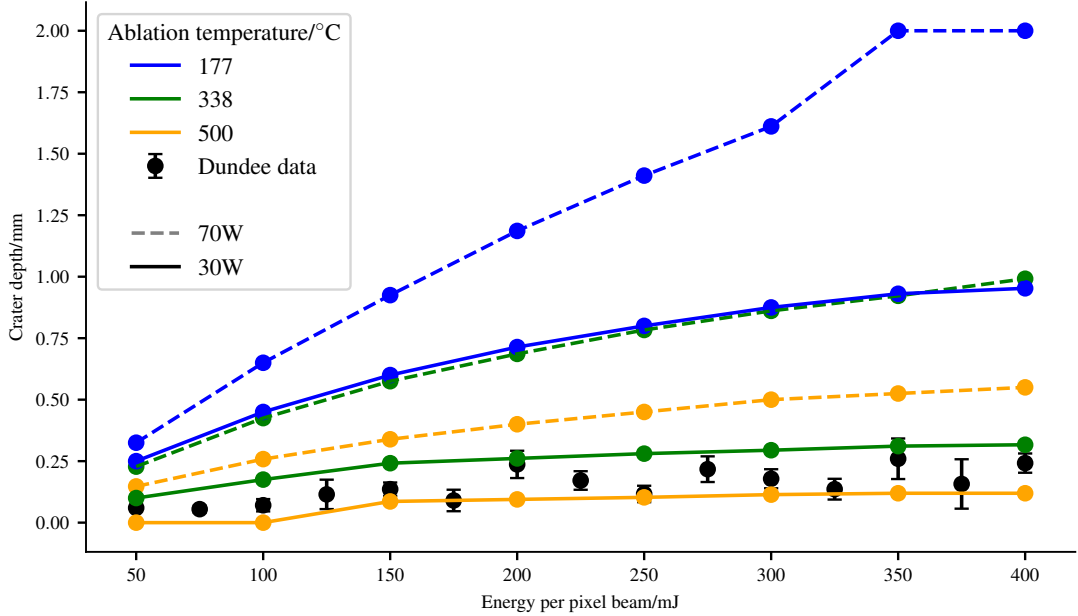


Figure 2.12: Simulations of 30 W and 70 W CO₂ ablative laser. Crater depths as a function of pixel beam energy for various T_a 's. *placeholder until I get 70W dundee data. need to rerun the upper 177 points on larger z depth as it crashes currently due to known error*

2.3.2 Results

2.3.2.1 Investigating ablation temperature, T_a

Various literature sources report the ablation temperature ranging from 177° to 500° [41, 42, 48]. Thus, we run several models over this range in order to establish a ‘good’ T_a which fits with the experimental results. Figure 2.12 shows how T_a affects the crater depth as a function of pixel beam energy for the CO₂ laser. Both the 70 W and 30 W simulations agree, that a ‘good’ T_a is around $T_a = 400$ °C.

Increasing the ablation temperature, has the obvious affect of requiring more energy to be deposited by the laser before ablation takes place. As more energy is required to heat the porcine tissue up to the ablation temperature before it can be ablated. This also allows more heat to diffuse away from the ablation crater increasing the thermal damage done to the surrounding tissue. Decreasing the ablation temperature has the converse affect, and allows the ablation crater to become deeper.

Over the full range of T_a , as the energy per pixel beam increases, there is a trend that at higher energies the crater depth tapers off. This is most likely due to a number of reasons. As the ablation craters grows the volume of tissue that is ablated is replaced with air, allowing more heat loss from the tissue to the environment. As well as heat loss to the environment, more heat is diffused away into the surrounding tissue as the crater grows, due to the availability of more tissue for the heat to diffuse into.

2.3.2.2 Investigating Thermal damage

As stated in Section 2.2.3.2, we use the Arrhenius damage integral in order to estimate the thermal damage due to the laser. In order to calculate the tissue damage around the ablation craters, we first transform Eq. (2.19) in to a summation:

$$\Omega(t) = \int_{t_i}^{t_f} A e^{-\frac{\Delta E}{RT}} d\tau \quad (2.39)$$

$$\Omega(t) = \sum_{m=m_i}^{m_f} A e^{-\frac{\Delta E}{RT_\xi^m}} \Delta t \quad (2.40)$$

Where:

ΔE , R , T , and A have the same meanings as before;

ξ is the i^{th} , j^{th} , k^{th} node;

and m_i is the i^{th} timestep when the ξ node is above the threshold temperature.

Using Eq. (2.40) we can thus estimate the damage to the tissue on a voxel by voxel basis. Figure 2.13 show how far the thermal damage extends around the ablation crater. For ease of visualisation we map 1-3 to their respective burns via the following scheme, with η as burn severity:

$$\eta = \begin{cases} 3, & \Omega \geq 10000 \\ 2, & 1 \leq \Omega < 10000 \\ 1, & 0.53 \leq \Omega < 1 \\ 0, & \Omega = 0. \end{cases} \quad (2.41)$$

As evidenced in Fig. 2.13, the thermal damage zone extends for a small distance around the ablation crater, due to the diffusion of heat into these areas. For the lower powered laser (30 W) there seems to be a maximum distance in how far the thermal damage extends beyond the ablation crater horizontally. Figure 2.14 show this cut-off which appears to start around 250 mJ .

In the higher powered laser (70 W), it appears that there is no upper cut-off for the maximum horizontal extent of thermal damage. The reason for this is that the simulated energies for the pixel beams were not large enough to reach the cut-off, and thus if more heat was deposited by the laser it would diffuse further into the tissue.

We can also investigate the time it takes for different areas of the tissue to become thermally damaged. This can be easily achieved by saving the time each voxel passes one of the damage boundaries in Eq. (2.41). Figure 2.16 show the minimum time taken for 1^{st} , 2^{nd} , and 3^{rd} degree burns to occur for both 30 W and 70 W powered lasers as a function of depth. The 70 W laser shows that there is little to no time (upon the order of 0.5 ms) between 1^{st} and 2^{nd} degree burns, and a maximum of $\sim 0.02\text{ s}$ between 2^{nd} and 3^{rd} degree burns. The 30 W has a larger time differential between burn classifications, with a maximum of 0.02 s between 1^{st} and 2^{nd} degree burns and a maximum of 0.2 s between 2^{nd} and 3^{rd} degree burns.

2.3.2.3 Comparison to experimental work

The work below will possibly be done. If so it will be in 2019 if not needed for the paper

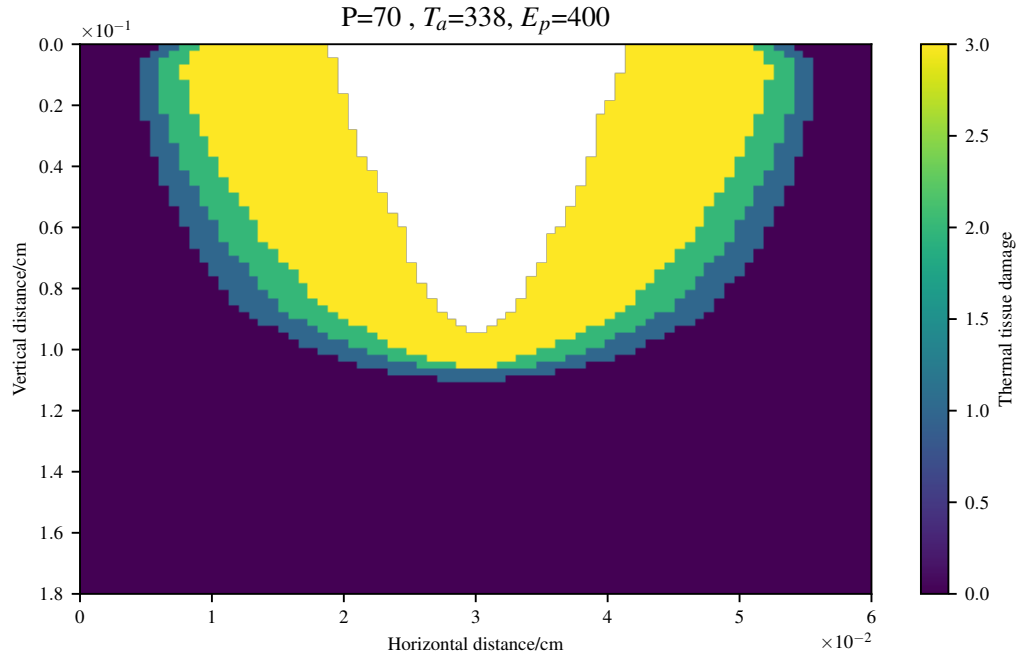


Figure 2.13: Tissue thermal damage around the ablation crater (white). Thermal tissue damage values of 3 refer to 3rd degree burns, 2 to 2nd, and 1 to 1st degree burns respectively. P is the power in Watts, T_a is the ablation temperature in Kelvin, and E_p is the energy per pixel beam in mJ *need to do this with more voxels*.

2.3.2.4 Effect of beam shape

2.3.2.5 Effect of thermal and optical properties on crater depth

As mentioned in the introduction to this section, the thermal and optical properties vary over a wide range in the literature. Thus there is no one ‘correct’ value we can choose for our simulations. In order to better understand how the thermal and optical properties affect the crater depth reached by the fractional laser, we vary the properties by 20%. This section presents the results of changing the thermal optical properties: heat capacity, thermal conductivity, protein and water absorption, and density.

Heat capacity, c_p

Thermal conductivity, κ

Absorption coefficient, μ_a

Density, ρ

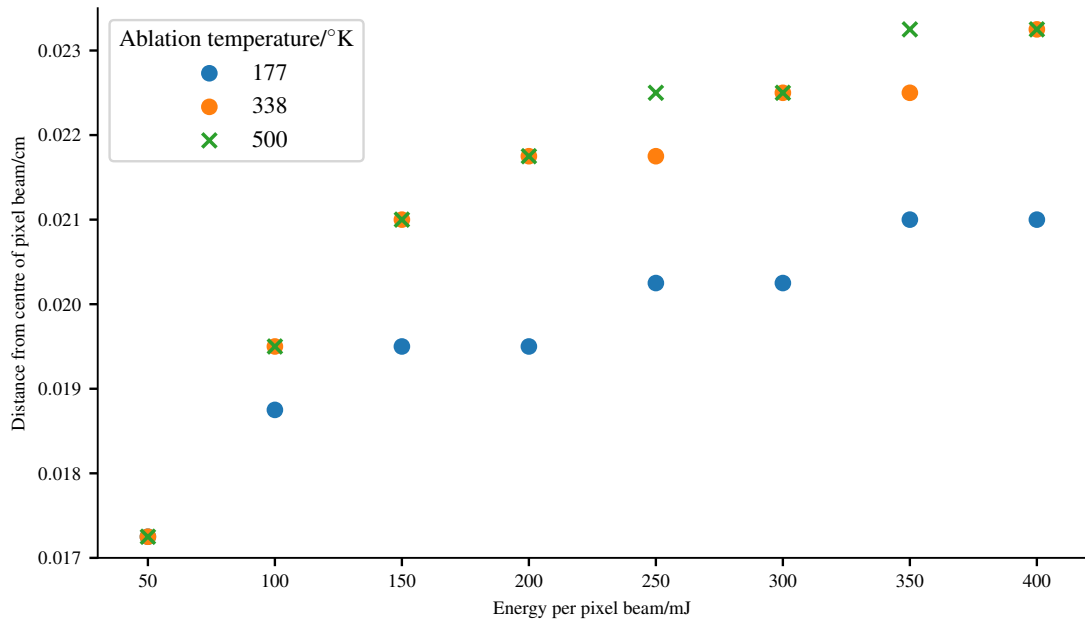


Figure 2.14: Figure shows the maximum horizontal extent of thermal damage as a function of energy per pixel beam for laser of power 30 W. Cut-off in thermal damage appears to set in around 250 mJ.

2.3.2.6 Investigating water content

2.3.2.7 Investigating temperature of air after ablation

2.4 Conclusion

Using MCRT and finite difference method, we have created a fully 3D model of photon and heat transport within tissue. This model can be used to simulate the heat deposited by laser, the ablation craters formed via high powered laser and the resultant thermal damage surrounding the ablation crater.

Our model has been fully validated against both analytical solutions and experimental results. We found that to match with experimental results that a tissue ablation temperature T_a of around 420 K has to be adopted.

The simulations allow us to predict for a given laser power and pulse length, how much thermal damage is caused in the tissue, and how deep an ablation crater that will form.

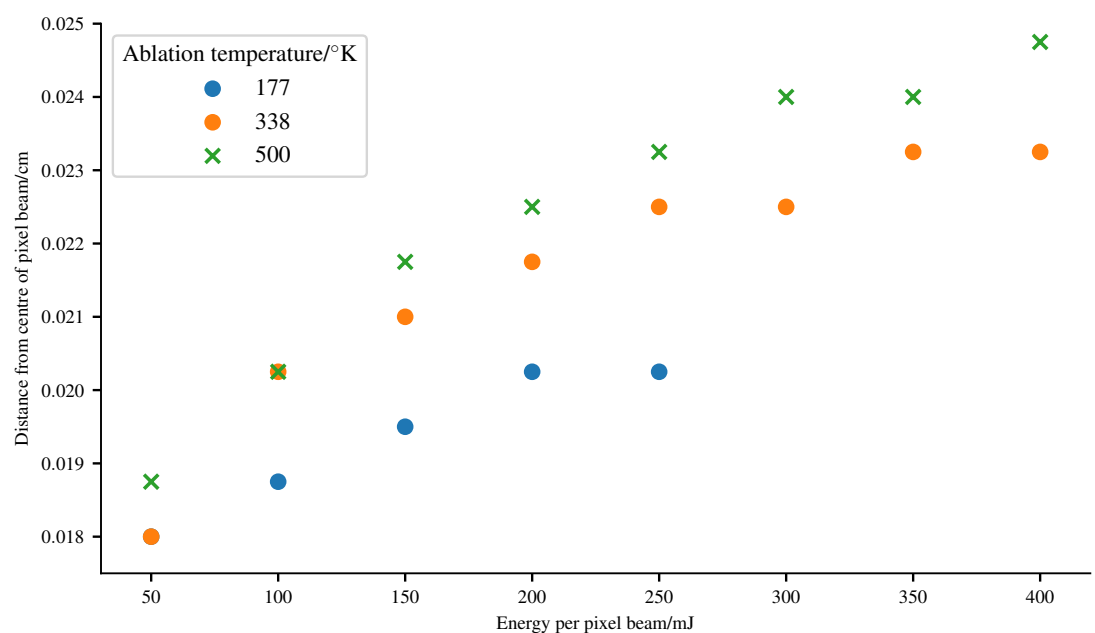


Figure 2.15: Figure shows the maximum horizontal extent of thermal damage as a function of energy per pixel beam for laser of power 70 W. There appears to be not cut-off in the horizontal extent of the thermal damage. *need to do this with more voxels*

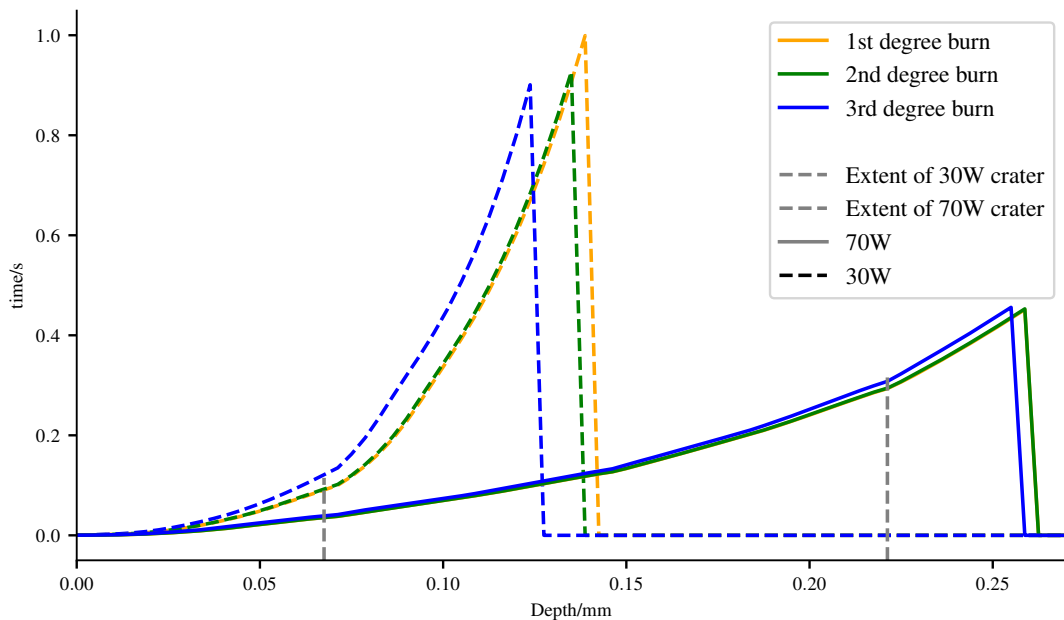


Figure 2.16: Figure shows the extent of burns inflicted by the laser as a function of depth. Lines are taken from the central point of the laser beam through the tissue. Coloured dashed lines are 30W laser and solid coloured lines are 70W laser.

Bibliography

- [1] Ashley J Welch, Martin JC Van Gemert, et al. *Optical-thermal response of laser-irradiated tissue*, volume 2. Springer, 2011.
- [2] David J Segelstein. *The complex refractive index of water*. PhD thesis, University of Missouri-Kansas City, 1981.
- [3] Lee Badger. Lazzarini’s lucky approximation of π . *Mathematics Magazine*, 67(2):83–91, 1994.
- [4] Petr Beckmann. *A history of Pi*. St. Martin’s Griffin, 2015.
- [5] Georges-Louis Leclerc Buffon. *Histoire naturelle générale et particulière*, volume 18. de l’Imprimerie de F. Dufart, 1785.
- [6] Peter Jäckel. *Monte Carlo methods in finance*. J. Wiley, 2002.
- [7] David B Hertz. Risk analysis in capital investment. *Harvard Business Review*, 42(1):95–106, 1964.
- [8] Jasper Vivian Wall and Charles R Jenkins. *Practical statistics for astronomers*. Cambridge University Press, 2012.
- [9] James T. Kajiya. The rendering equation. *SIGGRAPH Comput. Graph.*, 20(4):143–150, August 1986.
- [10] Robert L. Cook, Thomas Porter, and Loren Carpenter. Distributed ray tracing. *SIGGRAPH Comput. Graph.*, 18(3):137–145, January 1984.
- [11] Nicholas Metropolis. The beginning of the Monte Carlo method. *Los Alamos Science*, 15:125–130, 1987.
- [12] Roger Eckhardt. Stan Ulam, John von Neumann, and the Monte Carlo method. *Los Alamos Science*, 15:131–136, 1987.
- [13] HL Anderson. Metropolis, Monte Carlo, and the MANIAC. *Los Alamos Science*, 14:96–108, 1986.
- [14] Stanislaw Ulam, RD Richtmyer, and J Von Neumann. Statistical methods in neutron diffusion. *LAMS-551, Los Alamos National Laboratory*, pages 1–22, 1947.
- [15] Kenneth Wood and RJ Reynolds. A model for the scattered light contribution and polarization of the diffuse $h\alpha$ galactic background. *The Astrophysical Journal*, 525(2):799, 1999.

- [16] DWO Rogers, BA Faddegon, GX Ding, C-M Ma, J We, and TR Mackie. Beam: a monte carlo code to simulate radiotherapy treatment units. *Medical physics*, 22(5):503–524, 1995.
- [17] BC Wilson and G Adam. A monte carlo model for the absorption and flux distributions of light in tissue. *Medical Physics*, 10(6):824–830, 1983.
- [18] Saeid Amini-Nik, Darren Kraemer, Michael L Cowan, Keith Gunaratne, Puvindran Nadesan, Benjamin A Alman, and RJ Dwayne Miller. Ultrafast mid-ir laser scalpel: protein signals of the fundamental limits to minimally invasive surgery. *PLoS One*, 5(9):e13053, 2010.
- [19] Oon Tian Tan, Karen Sherwood, and Barbara A Gilchrest. Treatment of children with port-wine stains using the flashlamp-pulsed tunable dye laser. *New England journal of medicine*, 320(7):416–421, 1989.
- [20] Marina Kuperman-Beade, Vicki J Levine, and Robin Ashinoff. Laser removal of tattoos. *American journal of clinical dermatology*, 2(1):21–25, 2001.
- [21] Se Hwang Liew. Laser hair removal. *American journal of clinical dermatology*, 3(2):107–115, 2002.
- [22] Christina A Hardaway and E Victor Ross. Nonablative laser skin remodeling. *Dermatologic clinics*, 20(1):97–111, 2002.
- [23] Stanley M Shapshay, M Stuart Strong, Gaspar W Anastasi, and Charles W Vaughan. Removal of rhinophyma with the carbon dioxide laser: a preliminary report. *Archives of Otolaryngology*, 106(5):257–259, 1980.
- [24] Roberto Valcavi, Fabrizio Riganti, Angelo Bertani, Debora Formisano, and Claudio M Pacella. Percutaneous laser ablation of cold benign thyroid nodules: a 3-year follow-up study in 122 patients. *Thyroid*, 20(11):1253–1261, 2010.
- [25] Merete Hædersdal, Fernanda H Sakamoto, William A Farinelli, Apostolos G Doukas, Josh Tam, and R Rox Anderson. Fractional co2 laser-assisted drug delivery. *Lasers in Surgery and Medicine: The Official Journal of the American Society for Laser Medicine and Surgery*, 42(2):113–122, 2010.
- [26] Dieter Manstein, G Scott Herron, R Kehl Sink, Heather Tanner, and R Rox Anderson. Fractional photothermolysis: a new concept for cutaneous remodeling using microscopic patterns of thermal injury. *Lasers in Surgery and Medicine: The Official Journal of the American Society for Laser Medicine and Surgery*, 34(5):426–438, 2004.
- [27] Rong Kong, Martin Ambrose, and Jerome Spanier. Efficient, automated monte carlo methods for radiation transport. *Journal of computational physics*, 227(22):9463–9476, 2008.
- [28] Gang Yao and Lihong V Wang. Monte carlo simulation of an optical coherence tomography signal in homogeneous turbid media. *Physics in Medicine & Biology*, 44(9):2307, 1999.
- [29] AJ Welch, Craig Gardner, Rebecca Richards-Kortum, Eric Chan, Glen Criswell, Josh Pfefer, and Steve Warren. Propagation of fluorescent light. *Lasers in Surgery and Medicine: The Official Journal of the American Society for Laser Medicine and Surgery*, 21(2):166–178, 1997.

- [30] Catherine Louise Campbell, Kenny Wood, RM Valentine, C Tom A Brown, and H Moseley. Monte carlo modelling of daylight activated photodynamic therapy. *Physics in Medicine & Biology*, 60(10):4059, 2015.
- [31] David A Boas, JP Culver, JJ Stott, and AK Dunn. Three dimensional monte carlo code for photon migration through complex heterogeneous media including the adult human head. *Optics express*, 10(3):159–170, 2002.
- [32] Sachin V Patwardhan, Atam P Dhawan, and Patricia A Relue. Monte carlo simulation of light-tissue interaction: three-dimensional simulation for trans-illumination-based imaging of skin lesions. *IEEE transactions on biomedical engineering*, 52(7):1227–1236, 2005.
- [33] Kenneth Wood, LM Haffner, RJ Reynolds, John S Mathis, and Greg Madsen. Estimating the porosity of the interstellar medium from three-dimensional photoionization modeling of h ii regions. *The Astrophysical Journal*, 633(1):295, 2005.
- [34] Isla Rose Mary Barnard, Patrick Tierney, Catherine Louise Campbell, Lewis McMillan, Harry Moseley, Ewan Eadie, Christian Tom Alcuin Brown, and Kenneth Wood. Quantifying direct dna damage in the basal layer of skin exposed to uv radiation from sunbeds. *Photochemistry and photobiology*.
- [35] LB Lucy. Computing radiative equilibria with monte carlo techniques. *Astronomy and Astrophysics*, 344:282–288, 1999.
- [36] Necati Ozisik. *Finite difference methods in heat transfer*. CRC press, 1994.
- [37] Gene M Amdahl. Validity of the single processor approach to achieving large scale computing capabilities. In *Proceedings of the April 18-20, 1967, spring joint computer conference*, pages 483–485. ACM, 1967.
- [38] Markolf H Niemz. *Laser-tissue interactions: fundamentals and applications*. Springer Science & Business Media, 2013.
- [39] Francesco Petrella, Sergio Cavaliere, and Lorenzo Spaggiari. Popcorn effect. *Journal of bronchology & interventional pulmonology*, 20(2):193–194, 2013.
- [40] Alfred Vogel and Vasan Venugopalan. Mechanisms of pulsed laser ablation of biological tissues. *Chemical reviews*, 103(2):577–644, 2003.
- [41] Miron Gerstmann, Y Linenberg, Abraham Katzir, and Solange Akselrod. Char formation in tissue irradiated with a CO₂ laser: model and simulations. *Optical Engineering*, 33(7):2343–2352, 1994.
- [42] Alan L McKenzie. A three-zone model of soft-tissue damage by a CO₂ laser. *Physics in Medicine & Biology*, 31(9):967, 1986.
- [43] John A Pearce. Relationship between arrhenius models of thermal damage and the cem 43 thermal dose. In *Energy-based Treatment of Tissue and Assessment V*, volume 7181, page 718104. International Society for Optics and Photonics, 2009.
- [44] FC Jr Hendriques. Studies of thermal injury; the predictability and the significance of thermally induced rate processes leading to irreversible epidermal injury. *Arch. Pathol.(Chic)*, 43:489–502, 1947.

- [45] SC Jiang, N Ma, HJ Li, and XX Zhang. Effects of thermal properties and geometrical dimensions on skin burn injuries. *Burns*, 28(8):713–717, 2002.
- [46] KR Diller and LJ Hayes. A finite element model of burn injury in blood-perfused skin. *Journal of biomechanical engineering*, 105(3):300–307, 1983.
- [47] Bernard Choi and Ashley J Welch. Analysis of thermal relaxation during laser irradiation of tissue. *Lasers in Surgery and Medicine: The Official Journal of the American Society for Laser Medicine and Surgery*, 29(4):351–359, 2001.
- [48] Aharon Sagi, Ariella Avidor-Zehavi, Avraham Shitzer, Miron Gerstmann, Solange Akselrod, and A Katzir. Heating of biological tissue by laser irradiation: temperature distribution during laser ablation. *Opt. Eng*, 31(7):1425–1431, 1992.